An Exchange Coupled meso-meso Linked Vanadyl Porphyrin Dimer for Quantum Information Processing

Davide Ranieri,† [a] Fabio Santanni,† [a] Alberto Privitera,[a] Andrea Albino,[a] Enrico Salvadori,[b] Mario Chiesa,[b] Federico Totti,[a] Lorenzo Sorace,* [a] and Roberta Sessoli[a]

---

a. Department of Chemistry "Ugo Schiff" & INSTM RU University of Florence Via della Lastruccia 3, 50019 Sesto Fiorentino, Italy

b. Department of Chemistry and NIS University of Turin Via P. Giuria 7, I10125 Torino, Italy

† These authors contributed equally to this work

* Corresponding author

Electronic Supplementary Information

S.1 Synthetic procedures

General remarks

The Porphyrin ligand, H_2TrPP, was purchased from PorphyChem SAS and used without further purification. The [VO(acac)$_2$] (Sigma-Aldrich, Merck) and PIFA (Alpha Aesar) reagents were employed as such. Commercially available dry CH_2Cl_2 was purchased from Sigma-Aldrich (Merck) and used without further treatment. All the manipulations and synthesis requiring an inert atmosphere were carried out with standard Schlenk techniques using N_2 as the inert gas. All glassware was previously dried by warming in an oven at 110 °C and vacuum pumped before use.

Synthesis of [VO(TrPP)]. The general synthesis was readapted from the literature.[1] Phenol (PhOH, 2 g) was heated to 80 °C and degassed by vacuum/N2 cycles in a pre-dried flask. H_2TrPP (80 mg, 0.15 mmol) and VO(acac)$_2$ (40 mg, 0.15 mmol) were added to the PhOH solution, and the reaction mixture was heated to 165 °C under N_2 for 12 h. The reaction was checked by TLC (CH_2Cl_2/Pet. ether 1:1) and UV/Vis (**Figure S15**). Afterward, PhOH was removed by distillation under a constant N_2-flow, while the temperature was kept at 140 °C – 150 °C. The crude product was then solved in 200 mL of CH_2Cl_2, filtered, and purified by column chromatography (flash silica gel, CH_2Cl_2/Pet. ether 1:1). The overall process yielded 50 mg (0.08 mmol) of a microcrystalline powder identified as the target **[VO(TrPP)]** product (final yield = 55%). R_f (CH_2Cl_2/Pet. ether 1:1) = 74%; λ_{max}(CH_2Cl_2) = 417 nm, 541 nm, 576 nm; v_{max}/cm^{-1}: 3101 (w), 3052 (w), 3029 (w), 2921 (vw), 2852 (vw), 2363 (w), 2332(w), 1588 (w), 1492(w), 1442 (m), 1376 (w), 1324(m), 1075 (m), 1000 (vs, V=O stretching), 952(vs), 853 (m), 801 (s), 756 (s), 721 (s), 697 (s), 659 (w). MALDI-MS (m/z): 603.13 ($M^{\cdot+}$). X-ray quality crystals were obtained as reported in Results. The experimental PXRD pattern obtained by measuring the microcrystalline powder was compared with the simulated one (**Figure S5**).

Synthesis of [VO(TrPP)]$_2$. The synthesis was performed using a slightly modified procedure from.[2] In a pre-dried Schlenk flask, **[VO(TrPP)]** (60 mg, 0.10 mmol) was added and solved in 30 mL of dry CH_2Cl_2 under N_2. The solution was cooled down to -78°C with the aid of an acetone/N_2 bath. Then, a PIFA (86 mg, 0.20 mmol) solution in 10 mL of dry CH_2Cl_2 was slowly added to the reaction mixture. Once the addition was completed, the acetone/N_2 bath was removed, and the reaction mixture was brought to room temperature. After 40 min of stirring at room temperature, UV/Vis and TLC analyses confirmed the full conversion of the precursor. The reaction was subsequently quenched with a $NaBH_4$ (37 mg, 1.00 mmol) solution in 12 mL of MeOH. The resulting solution was further stirred for an extra 15 min. Afterward, deionized H_2O (20 mL) was added to the reaction mixture, and the organic phase was collected and washed twice with sat. $NaHCO_3$ solution (30 mL x 2). The combined water phases were further extracted three times with CH_2Cl_2 (30 mL) to recover the residual product. After drying the combined organic phases with anhydrous $NaSO_4$, CH_2Cl_2 was removed under reduced pressure. The crude product was purified by column chromatography (flash silica gel) using toluene as eluent. The overall procedure yielded 65 mg (0.47 mmol) of pure **[VO(TrPP)]$_2$**·$3C_7H_8$ (final yield = 94%) as a microcrystalline powder. We should mention that after the purification of the dimer by column chromatography adopting toluene as eluting solvent (see Experimental and Theoretical Methods), one always obtains microcrystalline powder samples of **m-[VO(TrPP)]$_2$**. Furthermore, faster crystallization from toluene or acetone/toluene solutions led to **m-[VO(TrPP)]$_2$**. The comparison between the experimental and simulated PXRD patterns (**Figure S6**) highlights that the cell parameters are comparable to those of **m-[VO(TrPP)]$_2$**. R_f (toluene) = 0.52; $\lambda_{max}(CH_2Cl_2)$ 308 nm, 422 nm, 456 nm, 556 nm, 594 nm; MALDI-MS (m/z): 1204.67 ($M^{\cdot+}$); v_{max}/cm^{-1}: 3055 w and 3020 w (C=C streching), 2960 m and 2854 m (CH_3 streching from co solvent), 1596 m (N=C streching), 1486 w, 1438 m, 1367 w, 1326 m, 1261 m, 1204 m, 1175 m, 1000 s (V=O streching), 803 s, 744 m, 729 s, 721 s, 696 s, 660 m, 444 m

S.2 X-ray crystallography

Single-crystal X-ray diffraction measurements were performed on a Bruker Kappa APEX-II DUO diffractometer using CuKα radiation (λ = 1.542 Å). The crystal was kept at 100.0 K during data collection. The structures were solved using the Olex2 software package[3] by the intrinsic phasing method (SHELXT).[4] The refinement was carried out by using a full matrix least-squares minimization method (SHELXL package).[4] All non-H atoms were refined with anisotropic displacement parameters. Graphical material was prepared using Mercury CSD 2022.2.0.[5] The experimental results are listed in **Table S1**. We must mention that the empirical number of H atoms reported in **Table S1** for **m-[VO(TrPP)]$_2$** (H_{46}) is lower than the theoretical one (H_{70}) since H atoms were not included for disordered toluene molecules. Powder X-ray diffraction (PXRD) patterns on polycrystalline samples of **[VO(TrPP)]** and **m-[VO(TrPP)]$_2$** were recorded on a Bruker New D8 Advance DAVINCI diffractometer in a θ−θ configuration equipped with a linear detector. The patterns were collected within the range 5−50° (2 *ϑ*) using CuKα radiation (*λ* = 1.5398 Å) with a step varying from 0.025° to 0.029° and an exposure time varying from 0.6 to 1 s/deg. Simulated patterns were generated from the atomic coordinates of the single-crystal structure solutions.[5]

The powdered samples employed for magnetic studies were characterized by powder X-ray diffractometry, and their patterns were coincident with those simulated from the **m-[VO(TrPP)]$_2$** structure (**Figure S6**).

Table S1. Most important crystallographic data obtained from single crystal X-ray diffraction analysis of **[VO(TrPP)]**, **m-[VO(TrPP)]$_2$**, and **o-[VO(TrPP)]$_2$**.[6]

Sample	**[VO(TrPP)]**	**m-[VO(TrPP)]$_2$**	**o-[VO(TrPP)]$_2$**
CCDC	2202805	2203175	2203176
Empirical Formula	$VON_4C_{38}H_{24}$	$V_2O_2N_8C_{97}H_{46}$	$V_2O_2N_8C_{76}H_{46}$
Formula weight (g mol^{-1})	603.58	1457.34	1205.11
Crystal system	monoclinic	monoclinic	orthorhombic
Space group	$P2_1/c$	$C2/c$	$Ccc2$
Z	4	4	4
a (Å)	18.9568(9)	29.2955(12)	20.8648(13)
b (Å)	8.0830(3)(2)	11.3883(5)	27.1717(13)
c (Å)	19.9282(9)	22.5512(9)	11.4881(6)
α (°)	90	90	90
β (°)	114.250(2)	96.942(2)	90
γ (°)	90	90	90
V (Å^3)	2784.1(2)	7468.5(5)	6513.0(6)
ρ (calc.) (Mg/m^3)	1.440	1.296	1.229
μ (mm^{-1})	3.294	2.557	2.816
T (K)	100	100	100
Radiation	CuK_α (λ = 1.514178 Å)	CuK_α (λ = 1.514178 Å)	CuK_α (λ = 1.514178 Å)
θ range (°)	2-56 – 68.36	3.95 – 68.54	5.33 – 72.83
F(000)	1244	2984	2480
GooF	1.066	1.104	1.049
$R1$ (%)[a]	8.31	6.38	7.33
$wR2$ (%)[a]	22.46	16.55	21.88
Intramolecular Porphyrin dihedral angle (°)	-	66	77
Intramolecular VO-VO torsion angle (°)	-	64	72
Intramolecular VO-VO distance (Å)	-	8.52	8.37
Intermolecular VO-VO distance (Å)	9.42	10.44	7.78

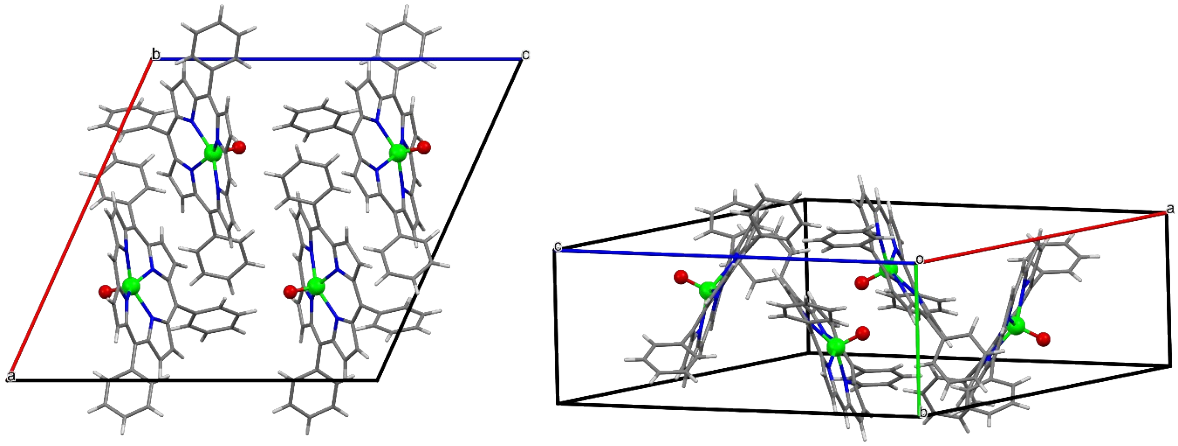

Figure S1. Crystal structure of **[VO(TrPP)]** viewed along the b-axis (left). On the right side of the figure, it is possible to see the two magnetically non-equivalent molecules in the cell. Color code: C = gray; H = white; N = blue; V = green; O = red.

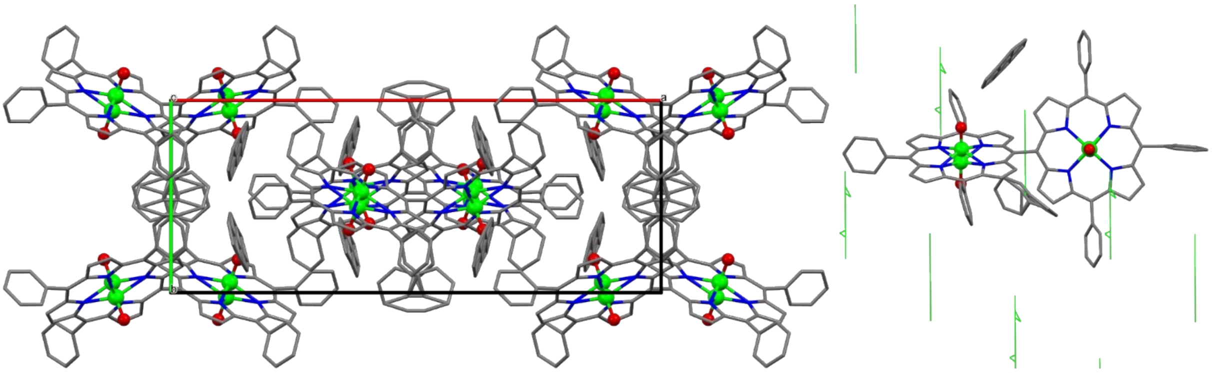

Figure S2. Crystal structure of **m-[VO(TrPP)]$_2$** viewed along the c-axis (left) and ball and stick model of **m-[VO(TrPP)]$_2$** (right). The disorder of two of the crystallization toluene molecules and vanadyl ions is visible in the figure on the right. The other toluene molecule is placed in correspondence with the crystallographic C_2 screw axis marked as a green line with two arrows. The C_2 fold axis is also indicated as a green line and cuts the porphyrin at the *meso-meso* C-C bond, creating an asymmetric unit containing only one-half of the porphyrin dimer. Color code: C = gray; N = blue; V = green; O = red.

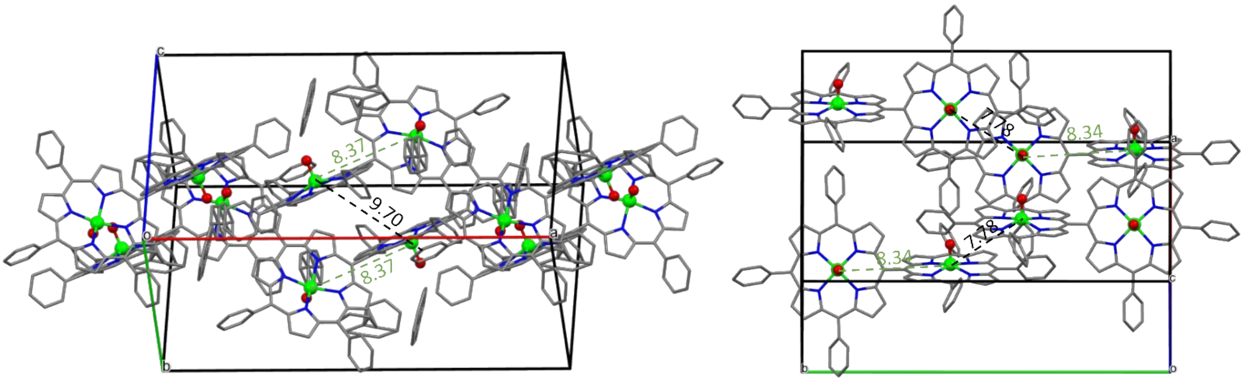

Figure S3. Unit cell content of **m-[VO(TrPP)]$_2$** (left) and **o-[VO(TrPP)]$_2$** (right) with the shortest inter (green dashed lines)-and intramolecular (black dashed lines) V-V distances in the crystal labeled. Color code: C = gray; N = blue; V = green; O = red.

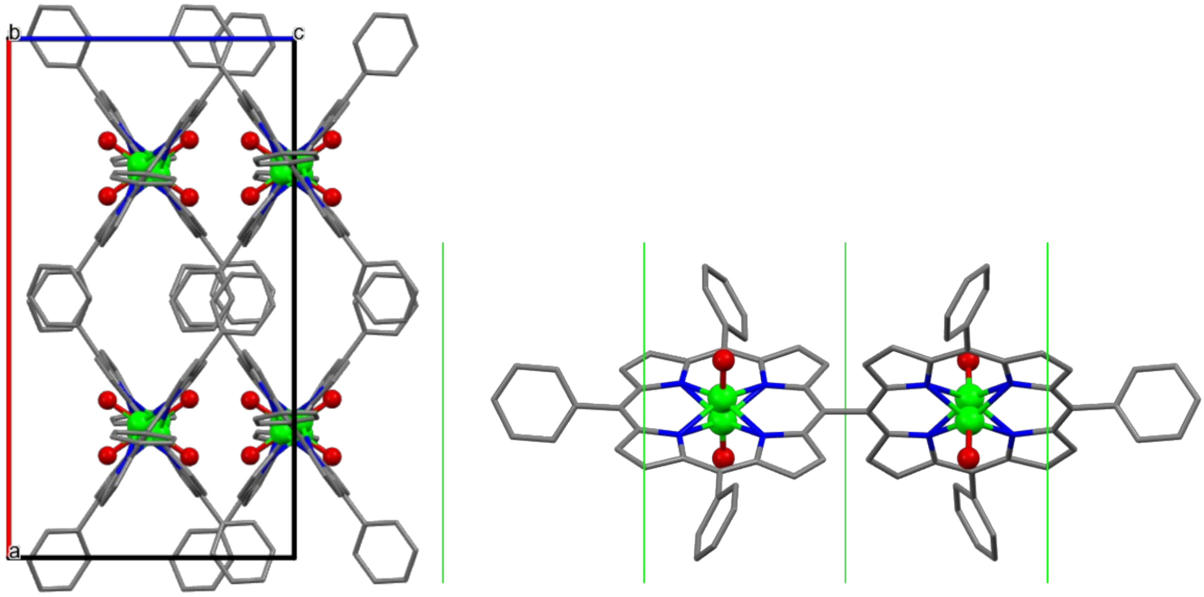

Figure S4. Content of the unit cell of **o-[VO(TrPP)]$_2$** viewed along the b-axis (left) and ball and stick model of a single molecule of **o-[VO(TrPP)]$_2$** (right). In this structure, the *meso-meso* C-C bond is along the b-axis. Similar to **m-[VO(TrPP)]$_2$**, we have two disordered Vanadyl-ions and a C_2-axis (green lines) that passes through the *meso-meso* linkage. Color code: C = gray; N = blue; V = green; O = red.

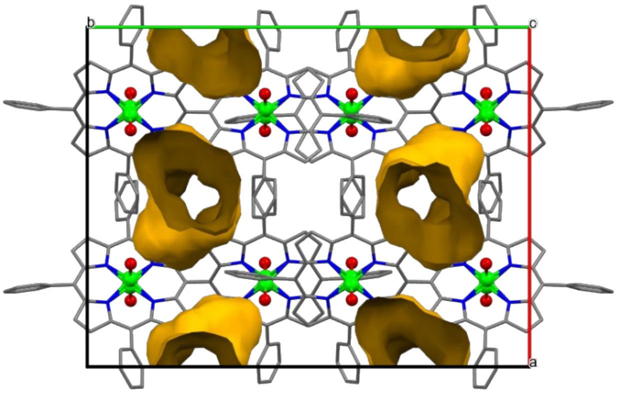

Figure S5. Content of the unit cell of **o-[VO(TrPP)]$_2$** viewed along the c-axis. From this point of view, the voids in the structures (brown surface) are visibl. Color code: C = gray; N = blue; V = green; O = red.

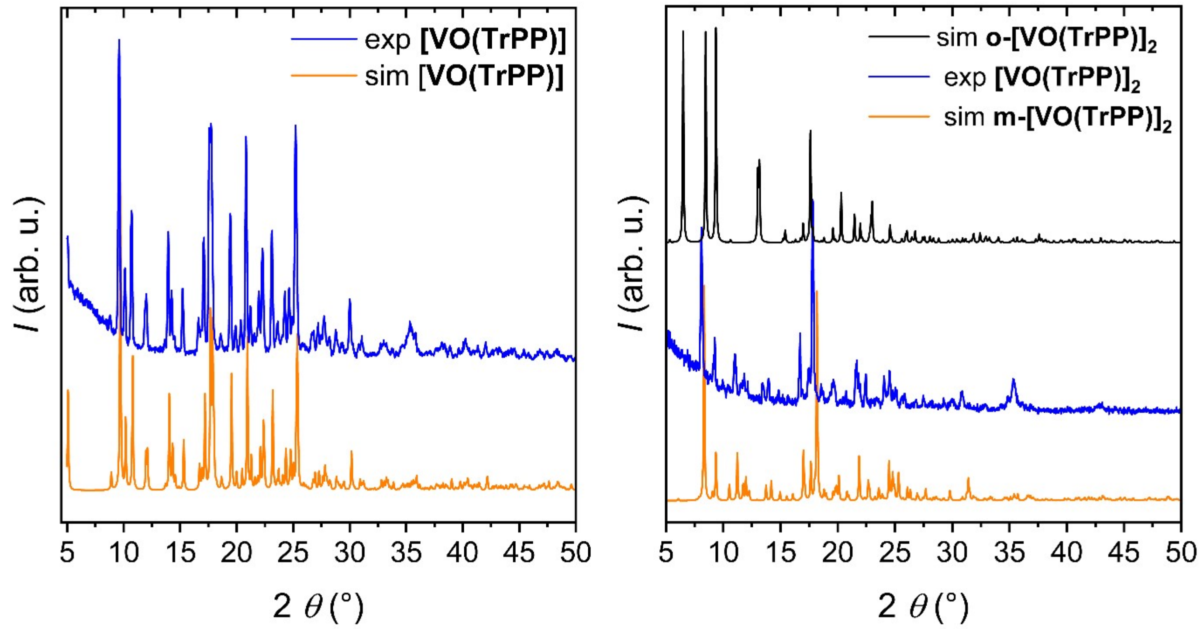

Figure S6. Simulated (orange) and experimental (blue) PXRD-pattern of **[VO(TrPP)]** (left), and **m-[VO(TrPP)]$_2$** (right). In addition to the simulated **m-[VO(TrPP)]$_2$** powder pattern, the simulated powder pattern of **o-[VO(TrPP)]$_2$** (black line) is reported in the right panel to highlight the difference between the two structures. Only **m-[VO(TrPP)]$_2$** powders are obtained by fast crystallization in toluene.

S.3 Electron Paramagnetic Resonance (EPR)

X-band CW-EPR spectra of all samples were recorded on a Bruker Elexsys E500 spectrometer equipped with an SHQ cavity ($\nu \cong 9.87$ GHz without cryostat, $\nu \cong 9.40$ GHz with cryostat). Low-temperature measurements were obtained using an Oxford Instruments ESR900 continuous flow helium cryostat and temperature-controlled by an Oxford Instrument ITC. A dedicated sample holder was used for single-crystal measurements, allowing a complete rotation (360°) of the sample around the horizontal axis. Single-crystal spectra were recorded by performing three different rotations along three reference axes orthogonal to each other. Spectra were recorded every 3° rotation from $\vartheta = 0°$ to $\vartheta = 180°$.Q-band pulsed EPR measurements were carried out with a Bruker Elexsys E580 at X-band ($\nu \cong 33.8$ GHz) equipped with a dielectric ring resonator (EN 5107D2) housed in an Oxford Instruments cryostat CF935. High-power microwave pulses were obtained using a 10 W solid-state amplifier. During the measurements, the resonator was overcoupled to minimize ringdown following the application of the microwave pulses. Temperatures between 4.5 and 50 K were obtained with an Oxford Instruments CF935 continuous flow helium cryostat. Echo-detected field-swept (EDFS) EPR spectra were recorded by using the Hahn Echo pulse sequence ($\pi/2-\tau-\pi-\tau-$echo) with fixed interpulse delay time $\tau = 200$ ns, $t_{\pi/2} = 40$ ns, and $t_{\pi} = 80$ ns. Phase memory times (T_m) were measured both by the Hahn Echo sequence upon increasing the interpulse delay τ starting from $\tau = 98$ ns and by a CPMG sequence with a fixed interpulse delay 2τ in the echo train and $\tau = 800$ ns. Typical pulse lengths were $t_{\pi/2} = 40$ ns and $t_{\pi} = 80$ ns. Spin−lattice relaxation times (T_1) were measured using the standard inversion recovery sequence ($\pi-t_d-\pi/2-\tau-\pi-\tau-$echo), with $\pi/2 = 16$ ns. The uncertainty in T_1 estimated from replicate measurements was 5−10% depending upon the signal-to-noise ratio at a given temperature field combination.

The acquired EPR spectra were simulated by using the core function *pepper* of the open-source MATLAB toolbox EasySpin.[7] The parameters included for the simulations of the **[VO(TrPP)]** monomer are the ***g*** and ***A*** tensors, which were assumed axial and collinear. The obtained values were subsequently fixed to perform the simulations of **[VO(TrPP)]$_2$** spectra, both single crystals, and frozen solution. In the simulations of the dimers, we took into account the tilting angle between the ***g*** and ***A*** tensors of the two VO units by including *Sys.gFrame* and *Sys.AFrame*. For the simulations of the single crystals (concentrated sample), we included the through-space dipolar interaction as a broadening of the linewidth, while we calculated the isotropic exchange coupling *J* by systematically varying its value from 0.001 ··10^{-2} to 100·· 10^{-2} cm^{-1} (**Figures S8** and **S9**). Conversely, for the spectrum of **[VO(TrPP)]$_2$** in frozen solution (diluted sample), besides the isotropic exchange *J*, we also calculated the through-space dipolar interaction ***D*** between the two VO units in the point-dipole approximation. All the simulation parameters are reported in **Table 1**.

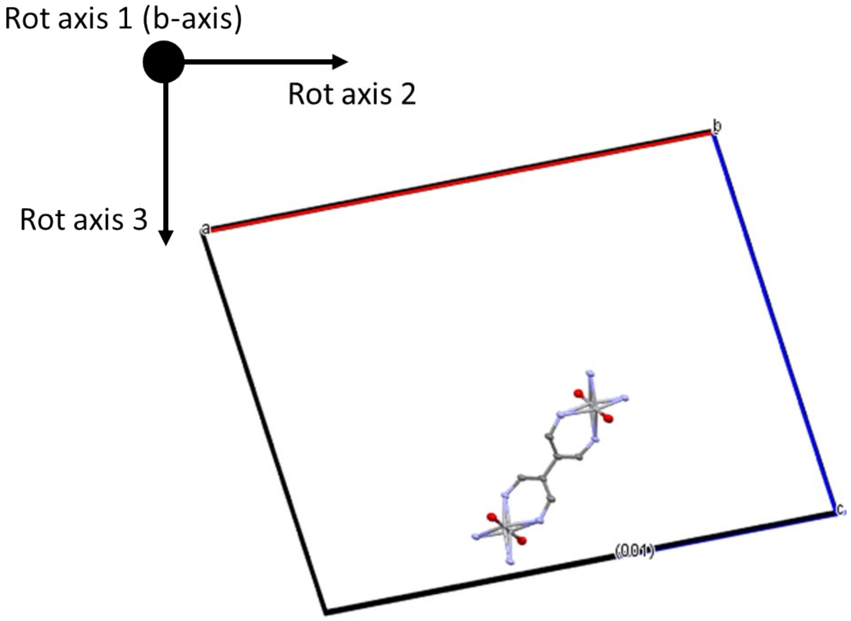

Figure S7. Rotations axes for the angular dependent cwEPR spectra of the **m-[VO(TrPP)]$_2$** crystal. Clockwise rotations were performed. Rotation axis 1 is parallel to the *b*-axis of the crystal. Rotation axis 2 is on the *ac* plane and is clockwise tilted by 14° with respect to the -*a* axis. Rotation axis 3 is on the *ac* plane and is clockwise tilted by 14° with respect to the *c*-axis

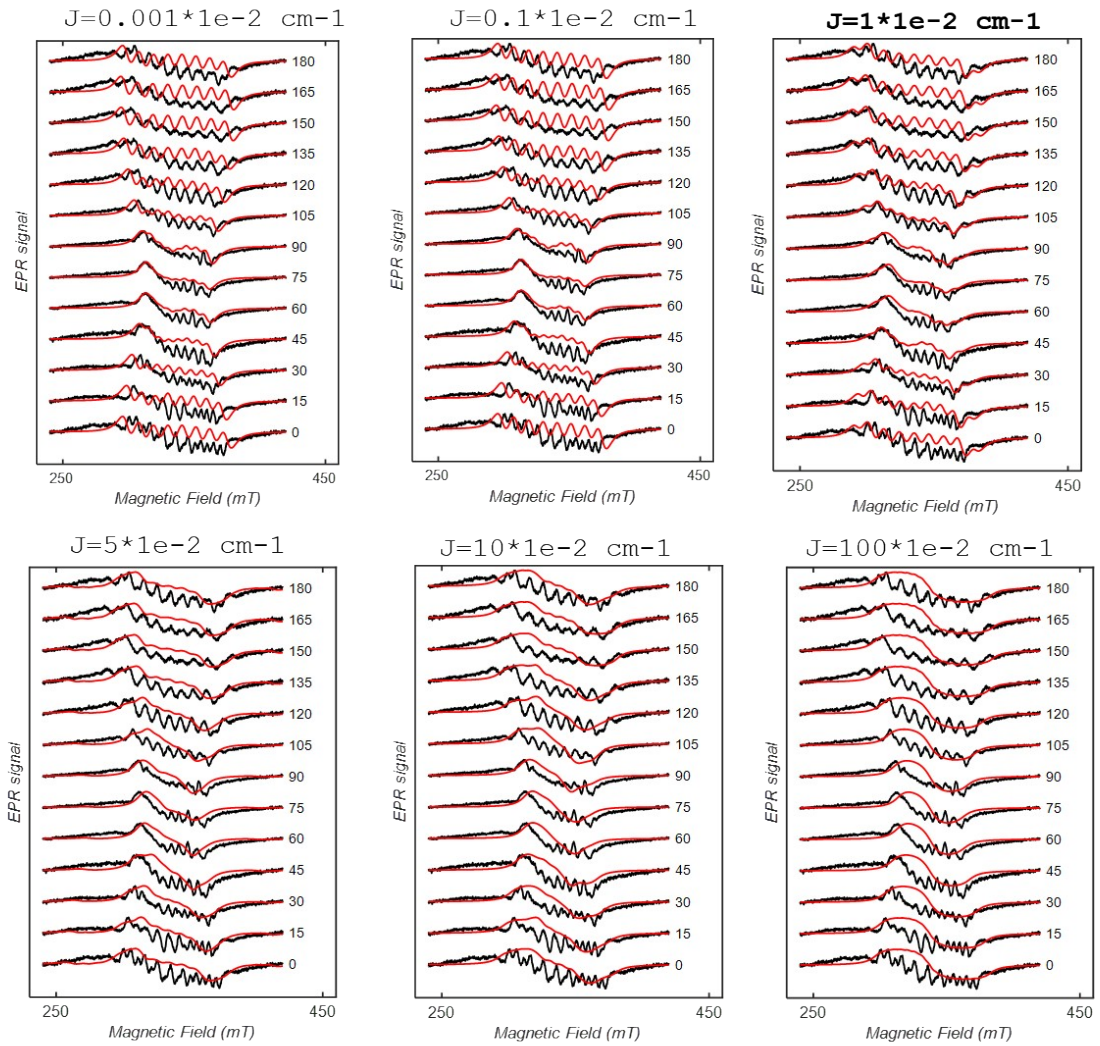

Figure S8. Simulations of the angular dependency of the EPR spectrum of the **m-[VO(TrPP)]$_2$** crystal for the rotation along the b-axis obtained by using different $|J_{12}|$ exchange coupling constants. In all cases, we assumed the same **g**- and **A**- tensors as the solution molecule. We considered the through-space dipolar interaction (both intra- and inter-molecular) as a linewidth broadening of 8 mT. The best agreement between data and simulations is obtained using $|J_{12}|$=0.01 (0.005) cm^{-1}.

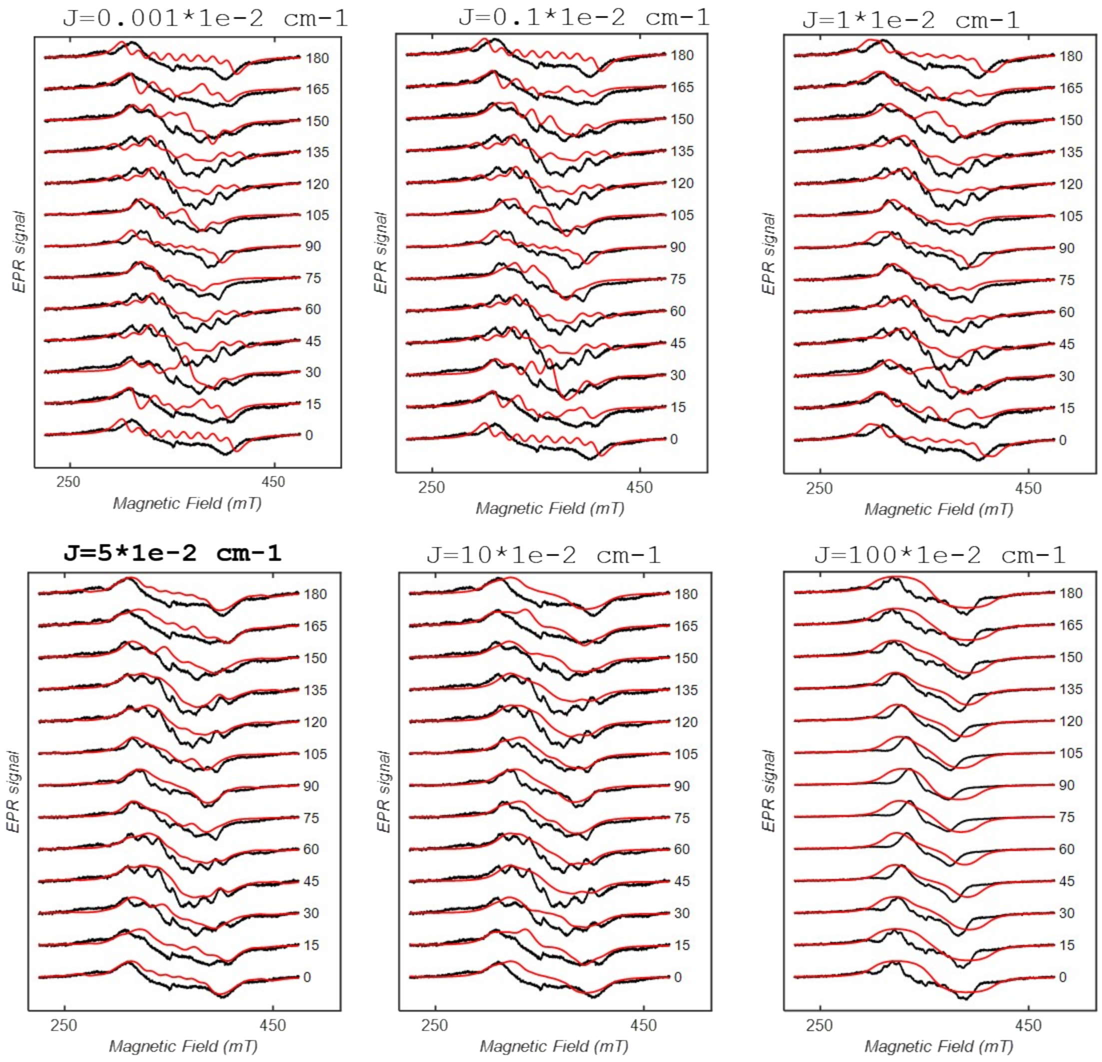

Figure S9. Simulations of the angular dependency of the EPR spectrum of the **o-[VO(TrPP)]$_2$** crystal for the rotation along the b-axis by using different $|J_{12}|$ exchange coupling constants. We considered the through-space dipolar interaction (both intra- and inter-molecular) as a linewidth broadening of 13 mT. The best agreement between data and simulations is obtained using $|J_{12}|$=0.05 (0.01) cm^{-1}.

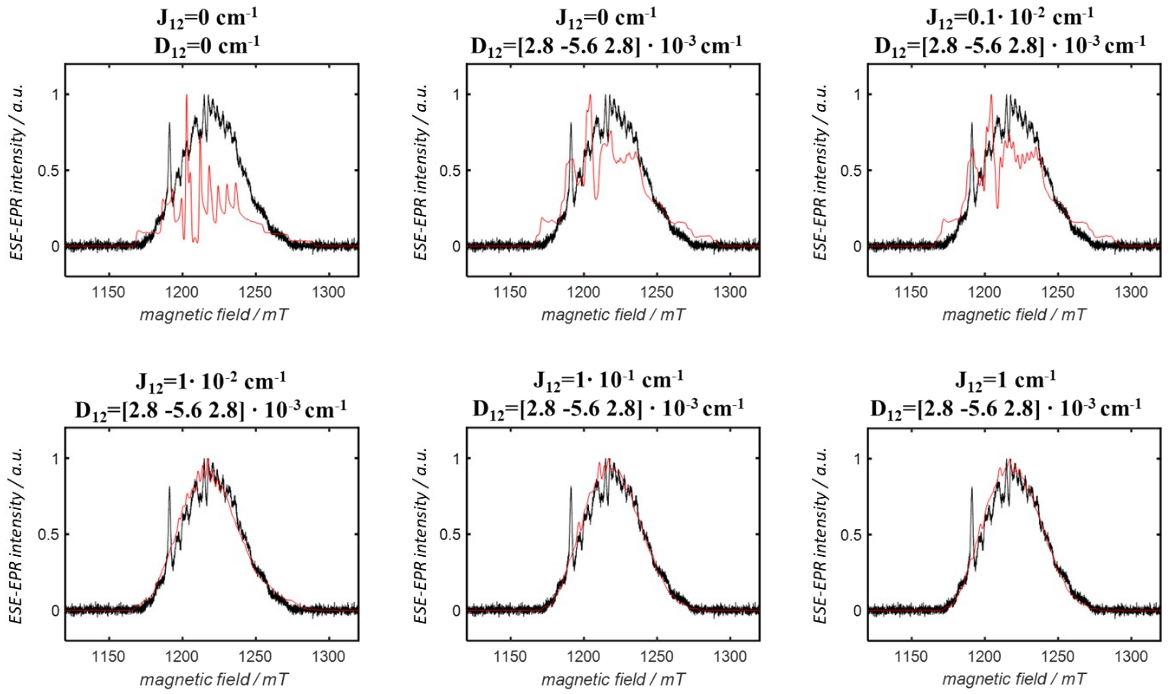

Figure S10. Experimental ESE-EPR spectrum (black line) of **[VO(TrPP)]$_2$** in frozen toluene solution (30 K) and spectral simulations (red lines) performed by varying both the isotropic exchange constant (J_{12}) and through-space dipolar coupling matrix (D_{12}). The results prove that both J_{12} and D_{12} should be included to obtain a good simulation of the experimental spectrum. Simulations are indistinguishable for $|J_{12}| > 1 \cdot 10^{-2}$ cm^{-1}, thereby providing a lower limit for the value of $|J_{12}|$.

Table S2: Experimental relaxation times (T_1 , T_m, and corresponding stretch parameters β_1, β_m) for **[VO(TrPP)]** and **[VO(TrPP)]$_2$** obtained from stretched-exponential fits of the Inversion Recovery experiment (T_1) and the Hahn Echo experiment (T_m). All samples were measured in frozen solution (0.5 mM d_8-toluene).

	[VO(TrPP)]				**[VO(TrPP)]$_2$**			
***T* (K)**	T_1 (μs)	β_1	T_m (μs)	β_m	T_1 (μs)	β_1	T_m (μs)	β_m
5	35500	0.65	1.8	0.7	3890	0.5	2.5	1
10	9578	0.66	2.8	0.8	1854	0.5	3.5	0.9
20	2504	0.6	5.3	1.5	1174	0.6	5.2	1
30	847	0.7	5.9	2.0	485	0.6	5.8	1
40	514	0.8	5.9	2.4	257	0.67	5.2	1
50	328	0.8	6.2	1.8	159	0.7	4.7	0.96

Table S3: Best fit parameters and uncertainties for the temperature dependence of T_1 obtained using eq. 4 in main text.

	[VO(TrPP]		**[VO(TrPP]$_2$**	
	Value	**Uncertainty**	**Value**	**Uncertainty**
a ($s^{-1}K^{-1}$)	2.1	1.5	49	5
b ($s^{-1}K^{-n}$)	0.5	0.3	2.8E-4	1.5E-3
n	2.2	0.2	4.2	1.4

S.4 DFT calculations details

The magnitude of the *J* values experimentally observed requires a computational approach that can limit even the tiny numerical errors introduced by convergence accelerators. Therefore, all the SCF have been performed without any of them and with no auxiliary basis sets. The convergence was set within an energy change of $1.0 \cdot 10^{-9}$ au, i.e., almost two orders of magnitudes tighter than the smallest experimental *J* value. Ab initio calculations were performed with the ORCA 5.0.3 package[8] with the B3LYP functional[9,10] and D3 as atom-pairwise dispersion correction[11,12] were tested employing all-electron basis sets: def2-TZVP basis set for the Cu, V, O, N, and C atoms and def2-SVP for H atoms, The molecular geometry used for these simulations was obtained from X-ray crystal data. Magneto-structural correlations were performed on the **o-[VO(TrPP)]$_2$** derivative by varying the dihedral ϑ angle from 17° to 157°. The Broken Symmetry (BS) approach has been used to calculate the isotropic exchange parameters, *J*, within the full projection method[13–15] by using eq. 1

$$J = \frac{[E(HS) - E(BS)]}{2S_1S_2} \quad (1)$$

where *E*(*HS*) and *E*(*BS*) correspond to the energies computed for the ferro- and antiferro-magnetically coupled V^{IV} ions. The S^2 values for both the high spin and BS states are reported in **Table S2** and indicate the correctness of the found solutions.

To verify the accuracy of the adopted method, a similar system for which the sign and the magnitude of the *J* value were experimentally determined was chosen: the triply linked Cu^{II}-porphyrin dimer **f-CuP2**,[16] with a *J* value of 3.84 cm^{-1}. The application of the chosen computational protocol led to a computed value of *J* of 5.63 cm^{-1}, confirming the requested accuracy both in sign and the order of magnitude to investigate the ones in the VO- porphyrin dimers. For the correspondent *m-m′* linked derivative, **CuP2**, with a structure similar to

[VO(TrPP)]$_2$, no experimental indications about the sign of the coupling were reported, given its very small value.

The X-ray structures have been used for both **o-** and **m-[VO(TrPP)]$_2$** and **f-CuP2**. Magneto-structural correlations were computed for the **m-[VO(TrPP)]$_2$**, varying the θ dihedral angle from 17° to 157°. For 17° ≤ θ < 90°, the two VO groups lay both above(below) the plane of the porphyrin, while one above and the other below for 90° < θ ≤ 157°.

Table S4. Energy and expectation S^2 values calculated for the **o-[VO(TrPP)]$_2$** as a function of ϑ values.

θ, degree	HS, a.u.	<S^2>	BS, a.u.	<S^2>
17	-5398.557565184	2.024198	-5398.557565643	1.024232
27	-5399.010004134	2.024065	-5399.010004391	1.024082
37	-5399.198347010	2.024012	-5399.198347191	1.024024
47	-5399.268445868	2.023945	-5399.268445987	1.023953
57	-5399.290966221	2.023873	-5399.290966313	1.023877
67	-5399.297448964	2.023806	-5399.297449057	1.023808
exp	-5399.298867348	2.023753	-5399.298867455	1.023754
87	-5399.298877464	2.023719	-5399.298877585	1.023718
97	-5399.298822488	2.023715	-5399.298822611	1.023715
107	-5399.298584630	2.023712	-5399.298584757	1.023712
117	-5399.297098614	2.023727	-5399.297098741	1.023728
127	-5399.290941862	2.023762	-5399.290941987	1.023728
137	-5399.269041377	2.02381	-5399.269041503	1.023816
147	-5399.197854853	2.023861	-5399.197854986	1.023869
157	-5398.991458461	2.023911	-5398.991458621	1.023922

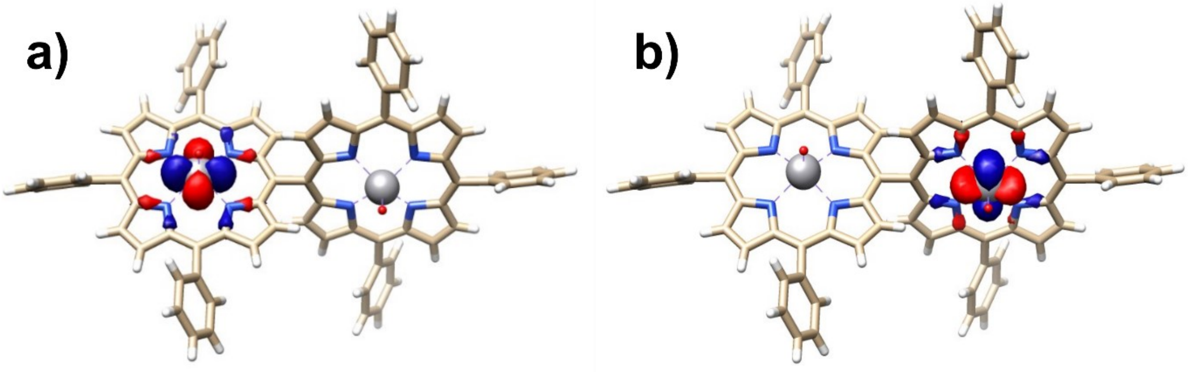

Figure S11. Magnetic orbitals computed for the **m-[VO(TrPP)]$_2$** with θ_{exp} (cutoff 0.03 au **a)** spin α; **b)** spin β

S.5 UV/Vis-Spectroscopy

UV-Vis measurements were performed on a Jasco V-670 spectrophotometer by using quartz cuvettes of 1 cm length.

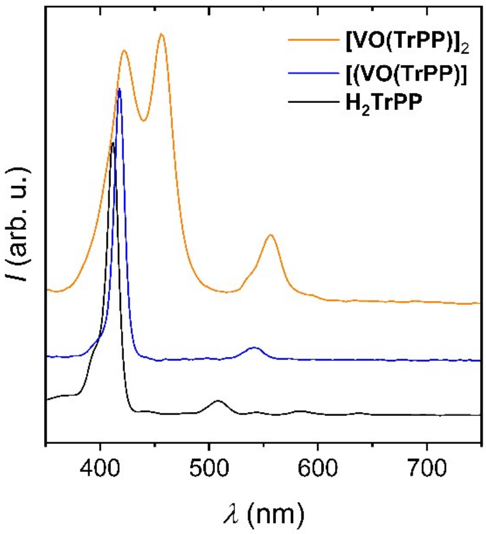

Figure S12. UV/Vis spectra of **[VO(TrPP)]$_2$** (orange line), **[VO(TrPP)]** (blue line) and H$_2$(TrPP) (black line).

S 6 Identification of computational states

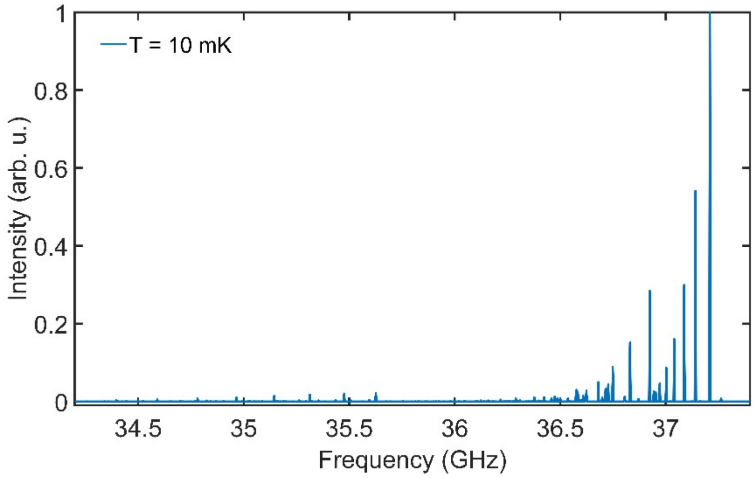

Figure S13. Simulated frequency-swept EPR spectrum of **o-[VO(TrPP)]$_2$** at *T* = 10 mK in a magnetic field of 1.3 T applied parallel to the local z-direction of one VO unit.

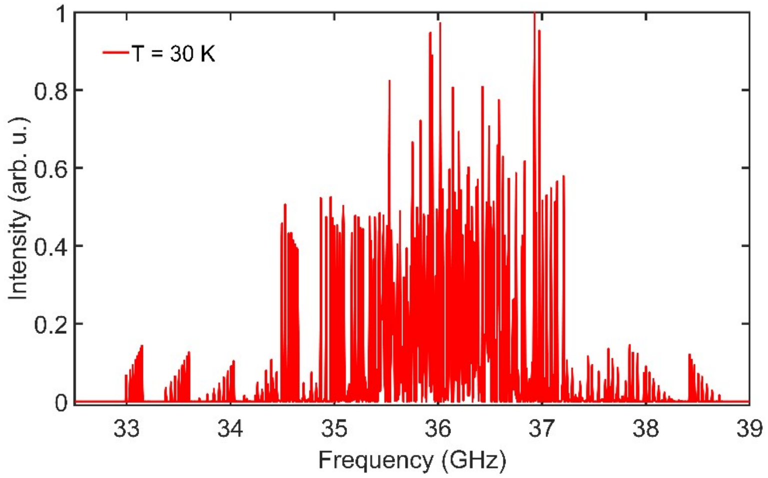

Figure S14. Simulated frequency-swept EPR spectrum of **o-[VO(TrPP)]$_2$** at *T* = 30 K in a magnetic field of 1.3 T applied parallel to the local z-direction of one VO unit.

References

1 T. Yamabayashi, M. Atzori, L. Tesi, G. Cosquer, F. Santanni, M.-E. Boulon, E. Morra, S. Benci, R. Torre, M. Chiesa, L. Sorace, R. Sessoli and M. Yamashita, *J. Am. Chem. Soc.*, 2018, **140**, 12090–12101.

2 Q. Ouyang, Y. Z. Zhu, C. H. Zhang, K. Q. Yan, Y. C. Li and J. Y. Zheng, *Org. Lett.*, 2009, **11**, 5266–5269.

3 O. V. Dolomanov, L. J. Bourhis, R. J. Gildea, J. A. K. Howard and H. Puschmann, *J. Appl. Cryst.*, 2009, **42**, 339–341.

4 G. M. Sheldrick, *Acta Cryst.*, 2015, **71**, 3–8.

5 C. F. MacRae, I. Sovago, S. J. Cottrell, P. T. A. Galek, P. McCabe, E. Pidcock, M. Platings, G. P. Shields, J. S. Stevens, M. Towler and P. A. Wood, *J. Appl. Cryst.*, 2020, **53**, 226–235.

6 *Dep. Numbers 2202805 (**[VO(TrPP]**) 2203176 (**o-[VO(TrPP]$_2$**) and 2203175 (**m-[VO(TrPP]$_2$**)* contain the cryst. data for this paper. These data are provided free of charge by the joint Cambridge Crystallographic Data Centre and Fachinformationszentrum Karlsruhe, 2022.

7 S. Stoll and A. Schweiger, *J. Magn. Reson.*, 2006, **178**, 42–55.

8 F. Neese, *Wiley Interdiscip. Rev. Comput. Mol. Sci.*, 2018, **8**, e1327.

9 A. D. Becke, *J. Chem. Phys.*, 1993, **98**, 5648–5652.

10 C. Lee, W. Yang and R. G. Parr, *Phys. Rev. B*, 1988, **37**, 785.

11 S. Grimme, J. Antony, S. Ehrlich and H. Krieg, *J. Chem. Phys.*, 2010, **132**, 154104–154123.

12 S. Grimme, S. Ehrlich and L. Goerigk, *J. Comput. Chem.*, 2011, **32**, 1456–1465.

13 L. Noodleman and J. G. Norman, *J. Chem. Phys.*, 1979, **70**, 4903–4906.

14 A. Bencini and F. Totti, *J. Chem. Theory Comput.*, 2009, **5**, 144–154.

15 C. Adamo, V. Barone, A. Bencini, F. Totti and I. Ciofini, *Inorg. Chem.*, 1999, **38**, 1996–2004.

16 N. Wili, S. Richert, B. Limburg, S. J. Clarke, H. L. Anderson, C. R. Timmel and G. Jeschke, *Phys. Chem. Chem. Phys.*, 2019, **21**, 11676–11688.